Environmental Science Nano

ROYAL SOCIETY OF CHEMISTRY

PAPER

Cite this: *Environ. Sci.: Nano*, 2023, **10**, 1828

Insights into Fenton-like oxidation of oxytetracycline mediated by Fe-doped porous g-C_3N_4 nanomaterials: synthesis, performance and mechanism†

Xiuqin Huo,[ab] Huan Yi,[ab] Eydhah Almatrafi,[b] Dengsheng Ma,[a] Yukui Fu,[a] Lei Qin,[a] Wu Xia,[a] Ling Xiang,[a] Fuhang Xu,[a] Huchuan Yan,[a] Chengyun Zhou,[ab] Guangming Zeng *[ab] and Cui Lai *[a]

Received 19th February 2023,
Accepted 13th May 2023

DOI: 10.1039/d3en00108c

rsc.li/es-nano

Photo-Fenton catalytic oxidation is considered economical and eco-friendly technology for energy development and environmental protection. However, high-performance catalysts are vital in this process. Thus, in this study, an Fe-doped porous g-C_3N_4 (Fe/PCN) nanomaterial was prepared *via* a one-step self-assembly strategy, which showed a large specific surface area, relatively negative conduction potential and intense visible light utilization, exhibiting an enhanced catalytic performance. As expected, in the photo-Fenton catalytic system, 99.24% oxytetracycline (OTC) degraded over Fe/PCN within 60 min, and the photo-Fenton degradation rate constant was up to 0.076 min^{-1}. Furthermore, a thimbleful of hydrogen peroxide (H_2O_2) could meet the requirement in this photo-Fenton reaction system. The catalytic mechanism of Fe/PCN was discussed in depth, where Fe/PCN not only activated H_2O_2 to generate hydroxyl radicals ($^{\cdot}OH$), but also photo-generated superoxide radicals ($^{\cdot}O_2^-$) due to its more negative conduction potential (–0.78 eV *vs.* NHE) than E^0 ($O_2/^{\cdot}O_2^-$) (–0.33 eV *vs.* NHE). Besides, the stability experiment showed that the precipitation of iron salts was prevented, which is conductive for practical applications. The possible degradation pathway of OTC was proposed and proven to be green according to the toxicity estimation software tool (TEST). The low consumption of H_2O_2, high tolerance to pH changes and coexisting ions and green degradation pathway of the prepared Fe/PCN make it a potential candidate for OTC removal. This work proposes a simple method to modulate the morphology and structure of g-C_3N_4 to enhance the catalytic activity of Fenton-like reactions.

Environmental significance

Due to the widespread detection of antibiotics and resistance genes in various water environments, water pollution caused by antibiotics has attracted increasing attention globally and become a research hotspot. In this case, photo-Fenton oxidation technology is considered a green and economical catalytic oxidation process for the control of antibiotic pollution in the environment. Nanomaterials have been widely used in photo-Fenton oxidation technology. This work presents a one-step self-assembly strategy to synthesize Fe-doped porous g-C_3N_4 (Fe/PCN) nanomaterials, which exhibit a relatively negative conduction potential, enhanced visible light utilization and more reaction active sites or channel. Fe/PCN displays a superior degradation efficiency for OTC in the photo-Fenton system, and thimbleful H_2O_2 can satisfy the requirement in this photo-Fenton reaction. Therefore, the prepared nano-catalyst can achieve the removal of organics with a reduced consumption of H_2O_2, making it economical and functional. Additionally, the nanomaterials present high tolerance to pH changes and coexisting ions. Besides, the stability experiment showed that the precipitation of iron salts was prevented, which is conductive for practical applications. The possible degradation pathway of OTC was proposed, which is proven to be green according to the toxicity estimation software tool (TEST).

1. Introduction

With the development of agriculture and aquaculture, abundant antibiotics are used to treat bacterial infections. Among them, oxytetracycline (OTC), a classic antibiotic, shows significant potential due to its broad spectrum and high efficiency.[1] However, most OTC is not absorbed, and subsequently released into the environment through feces or

[a] *College of Environmental Science and Engineering and Key Laboratory of Environmental Biology and Pollution Control (Ministry of Education), Hunan University, Changsha, 410082, PR China. E-mail: zgming@hnu.edu.cn, laicui@hnu.edu.cn; Fax: +86 731 88823701; Tel: +86 731 88822754*

[b] *Center of Research Excellence in Renewable Energy and Power Systems, Center of Excellence in Desalination Technology, Department of Mechanical Engineering, Faculty of Engineering-Rabigh, King Abdulaziz University, Jeddah 21589, Saudi Arabia*

† Electronic supplementary information (ESI) available. See DOI: https://doi.org/10.1039/d3en00108c

urine.[2] Consequently, water pollution caused by OTC poses a threat to human health and has become an urgent environmental problem to be addressed.[3] Accordingly, highly efficient and economic technologies are needed to remove OTC contaminant in water. Superoxide radicals ($^{\bullet}O_2^-$) generated from photocatalysis and hydroxyl radicals ($^{\bullet}OH$) generated from the Fenton process have attracted significant attention.[4] Photo-Fenton systems consisting of these two processes can exhibit superior catalytic activity. Photo-induced electrons can work with dissolved oxygen to produce $^{\bullet}O_2^-$ and decompose H_2O_2 into $^{\bullet}OH$,[5] which are conductive to the removal of organics. However, although H_2O_2-based AOPs show excellent potential for the efficient and green treatment of organics, the high cost for the production of H_2O_2 and its difficult transportation and storage restrict the development of this technology.[6] Therefore, reducing the consumption of H_2O_2 in the reaction process to realize the effective removal of organics has become a research focus.

Graphitized carbon nitride (g-C_3N_4) has been widely applied for the degradation of organics *via* photocatalysis because of its low cost, excellent stability and strong electron transport ability.[7] Nevertheless, its low specific area and insufficient visible light-harvesting capacity limit its photocatalytic performance.[8] Thus, efforts have been devoted to overcoming these shortcomings. For example, Zhu *et al.* designed oxygen-enriched g-C_3N_4, which improved the absorption of visible light.[9] Besides, doping heteroatom regulates the band gap of g-C_3N_4 and has been considered an efficient strategy to extend the absorption edge and restrain the photo-induced electron–hole recombination.[10] For instance, Miao *et al.* designed layered Fe-doped g-C_3N_4 with uniformly dispersed mesopores through pyrolysis, which showed enhanced photo-Fenton activity.[11] According to the results, it achieved 7.5-times higher catalytic performance compared with the untreated Fe–C_3N_4. Ma *et al.* synthesized Fe and Ti co-doped g-C_3N_4 to achieve an excellent performance for the degradation of OTC (0.05028 min^{-1}).[12] Liu *et al.* designed bio-inspired SACs by inserting pyrrole-type Fe–N_4 single sites into g-C_3N_4, which presented high tolerance to pH changes and low consumption of H_2O_2.[13] In addition, the catalytic activity also relies on a large specific surface area. In this case, porous structures have been considered a good way to enlarge the specific area of g-C_3N_4. In our previous research, we reviewed many strategies to form porous structures.[14] After modification, porous g-C_3N_4 (PCN) shows great potential in catalysis.

Therefore, design catalysts requiring a low consumption of H_2O_2 to realize the effective removal of organics is of great importance. In this study, an Fe-doped porous g-C_3N_4 (Fe/PCN) nanomaterial was firstly prepared by calcining a polymer consisting of ethylene diamine tetraacetic acid (EDTA) and hydrothermal-treated dicyandiamide (DCDA) and ferric chloride ($FeCl_3{\cdot}6H_2O$). Compared with the untreated dicyandiamide, hydrothermal-treated dicyandiamide as an oxygenated precursor exhibited a wider visible-light-responsive range.[15] Moreover, the addition of EDTA favored the self-assembly process due to the generation of a new precursor consisting of the weakly acidic EDTA and alkaline hydrothermal-treated DCDA. Doping Fe not only provided more active sites but also enhanced the visible light-harvesting capacity.[16] More importantly, the formation of Fe–N between the Fe species and PCN resulted in the enhanced activation of H_2O_2. Consequently, the prepared Fe/PCN exhibited a relatively negative conduction potential, enhanced visible light utilization and more reaction active sites. Fe/PCN was used to degrade OTC to investigate its photo-Fenton oxidation capacity. The superior OTC removal efficiency and high tolerance to pH changes and coexisting ions of this catalyst demonstrated its application potential. Moreover, a thimbleful of H_2O_2 could meet the requirement in this photo-Fenton reaction system, which is economical and effective. This work proposes a simple strategy for the fabrication of high-performance catalysts, which have potential for the removal of organics.

2. Materials and methods

2.1 Materials

The details of the materials used are presented in the ESI,† Text S1.

2.2 Preparation of Fe/PCN

Fe/PCN was synthesized *via* the following procedures. Firstly, 8 g of DCDA and 0.054 g of $FeCl_3{\cdot}6H_2O$ were added to a Teflon-lined high-pressure reactor (100 mL) with 60 mL deionized water. Subsequently, they were mixed and reacted in an oven at 180 °C for 4 h. After cooling to 30 °C, 0.4 g EDTA was added to the above solution and it was constantly stirred 0.5 h at 50 °C. Then, the obtained compound was collected, dried, and placed in a tinfoil-wrapped crucible and calcined for 2 h at 550 °C at a heating rate of 5 °C min^{-1}. Then, the compound was washed repeatedly with deionized water and ethanol. Finally, the product was obtained after drying at 60 °C. The product was denoted as 0.054Fe/PCN. PCN was synthesized using the same process without the addition of $FeCl_3{\cdot}6H_2O$. The *x*Fe/PCN (*x* represent the amount of added $FeCl_3{\cdot}6H_2O$) catalyst was obtained by adding different amounts $FeCl_3{\cdot}6H_2O$.

Some essential characterization methods, such as powder X-ray diffraction (XRD), scanning electron microscopy (SEM), transmission electron microscopy (TEM), Brunauer–Emmett–Teller (BET) method and X-ray photoelectron spectroscopy (XPS), were employed to illustrate the special feature of the prepared sample. The detailed information is listed in the ESI,† Text S2.

2.3 Catalytic test

The light source was a 300 W Xe lamp ($\lambda > 420$ nm, 155 mW cm^{-2}). As an antibiotic, OTC is difficult to remove because of its high chemical stability and poor biodegradability. Therefore, it is feasible to evaluate the catalytic performances

of the prepared sample by its OTC degradation efficiency. The detailed experimental process was as follows: 0.02 g 0.054Fe/PCN or other prepared sample was added to 0.1 L of OTC solution (10 mg L^{-1}), and then stirred for 0.5 h in the dark to realize adsorption/desorption equilibrium. After taking out the 0.003 L of the dark reaction solution, 5 mM H_2O_2 was added before exposure to light irradiation. In the photo-Fenton degradation process, 0.003 L of the reaction solution was taken out every 15 min and all the removed OTC solutions were filtered with a 0.22 μm filter membrane. Subsequently, the solution was quenched with 50 μL of *tert*butyl alcohol (TBA). Afterwards, the removed OTC solutions were measured to detect their characteristic peak at 353 nm using a Shimadzu UV-vis spectrophotometer (UV-2770). Also, the degradation intermediates were detected through liquid chromatography-mass (LC-MS) analysis. The detailed steps are presented in the ESI,† Text S3. Besides, HCl and NaOH were used to modulate the solution pH to investigate their influence. Additionally, the effects of inorganic salt ions were also determined. Finally, the used sample was washed repeatedly with deionized water and ethanol before its reuse.

2.4 Analytic methods

It is important to measure the photoelectrochemical properties of materials to determine their catalytic activity. Thus, the ultraviolet-visible (UV-vis) spectra of the prepared compounds were measured using a Varian Cary 300 spectrophotometer, scanning in the range of 200 to 800 nm with $BaSO_4$ as the reference material. An electrochemical workstation (CHI760E) was used to measure the transient photocurrent (IT) and electrochemical impedance spectroscopy (EIS). The parameters and conditions are shown in the ESI,† Text S4. Importantly, the electron spin resonance (ESR) signals of the radicals were detected using a JES FA200 spectrometer with 5,5-dimethyl-1-pyrroline-*n*-oxide (DMPO) as a scavenger. In addition, sodium oxalate (SO–2Na), 4-hydroxy-2,2,6,6-tetramethyl-piperidinooxy (TEMPO) and TBA were employed to monitor the holes (h^+), $\cdot O_2^-$ and $\cdot OH$, which may play a role in the degradation of OTC. An ICP-MS (Agilent 7700s) was used to detect the leaching of iron.

3. Results and discussion

3.1 Characterization

The crystal structure of the compound was tested by XRD. According to the XRD patterns of *x*Fe/PCN (Fig. 1a), the diffraction peaks in 27.4° and 12.8° correspond to the (002) and (100) crystal planes of g-C_3N_4, which are ascribed to the graphite-like stacked conjugated aromatic units and in-plane tri-*s*-thiazine repeating units, respectively.[17] The (002) peak became weaker and broader after Fe-doping, suggesting that Fe species affect the polymeric condensation.[5] Especially, the (100) peak disappeared, which may be due to the porous structure.[18] Besides, peaks assigned to Fe were absent, suggesting that Fe was chemically coordinated to g-C_3N_4, probably in the form of Fe–N bonds, without forming other complexes. The absence of foreign peaks suggested that the compound was highly pure. The SEM images are shown in

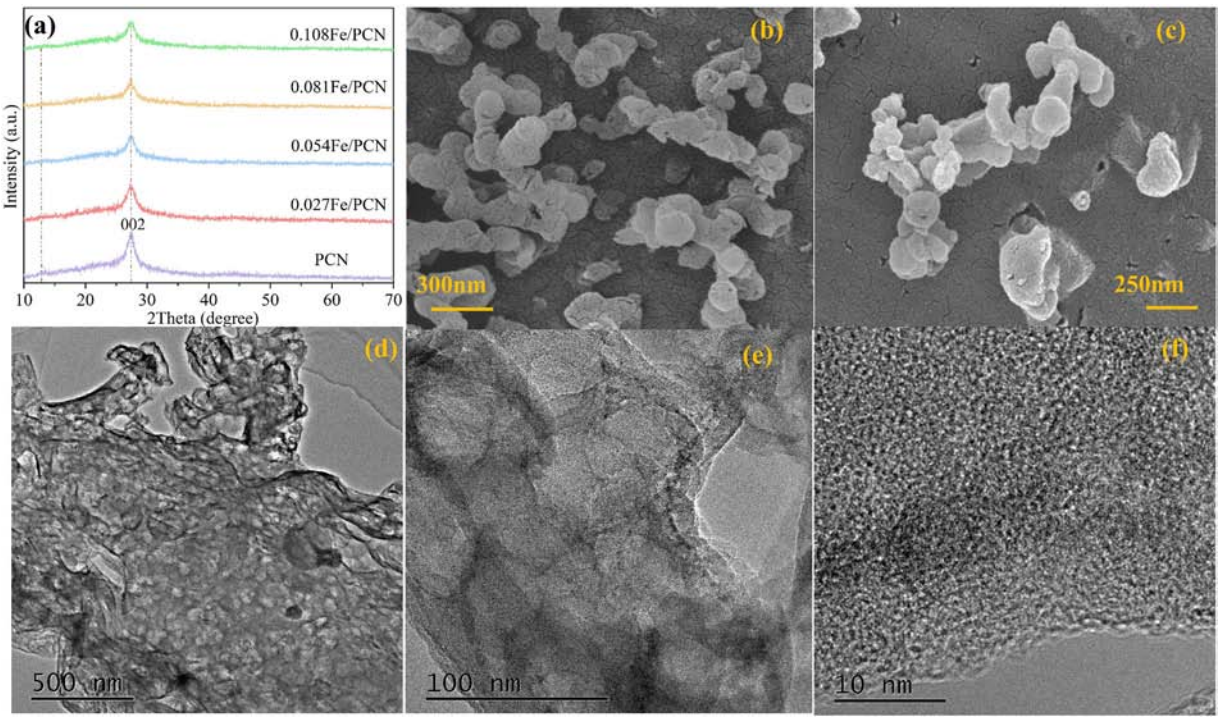

Fig. 1 (a) XRD patterns of PCN and *x*Fe/PCN. SEM images of (b) PCN and (c) 0.054Fe/PCN. TEM images of (d–f) 0.054Fe/PCN at different resolutions.

Fig. 1b and c, which show the morphology and microstructure of PCN and 0.054Fe/PCN. The surface of PCN exhibited cracks, which is probably because EDTA caused the sample morphology to be loosened.[16] As a structural reagent,[15,19] EDTA made the morphology of PCN become more regular (sheet structure with side length of 100 nm), which is ascribed to the strong complexation with the rich hydroxyl in EDTA. The morphology of 0.027Fe/PCN and 0.081Fe/PCN is showed in Fig. S1a and b,† which exhibited that the Fe species affected the creases on the surface. The TEM image of 0.054Fe/PCN is exhibited in Fig. 1d–f. It can be observed that the composites possess a porous structure. As shown in Fig. 1f, the absence of an obvious lattice fringe proved that iron did not form other compounds. Fe species were not observed in the TEM image but detected in the elemental mappings (Fig. S1c–f†), suggesting that Fe species may be doped in the g-C_3N_4 skeleton.

N_2 adsorption–desorption isotherms were measured to determine the specific surface areas and pore volumes of the prepared samples. According to Fig. 2a, mesopores were the main type of pores existing in 0.054Fe/PCN with the IUPAC-type IV pattern with H_3 hysteresis. The specific surface areas of PCN and 0.054Fe/PCN were determined to be 28.04 and 52.52 $m^2\ g^{-1}$, while their relative pore volumes were 0.13 and 0.26 $cm^3\ g^{-1}$, respectively. According to the BET analysis, Fe doping favored an enlargement in the specific surface area. Therefore, more active reaction sites are provided to facilitate the reaction, which was reflected by the adsorption performance. Besides, the micropores and mesopores of 0.054Fe/PCN were about 0.78 nm and 10.71 nm, respectively, suggesting its multi-hole morphology. Fig. S2† shows that the specific surface area of the pristine g-C_3N_4, which was formed by the direct calcination of DCDA, was about 9.69 $m^2\ g^{-1}$. The variation verified that EDTA occupied space during the thermal condensation and inhibited long-term polymerization, reconstructing the g-C_3N_4 precursor.[15]

Fig. 2b shows the FTIR spectra of PCN and 0.054Fe/PCN. In the spectrum of PCN, three obvious typical peaks were present. The peak at 805 cm^{-1} belongs to the breathing mode of the triazine units,[20] while the peaks observed at 3200–3500 cm^{-1} and 1200–1700 cm^{-1} are assigned to the stretching vibrations of the N–H group and aromatic C–N heterocycle units,[21,22] respectively. However, after doping Fe, a new absorption band appeared at 2150 cm^{-1}, belonging to the C≡N moiety, which was caused by the disturbance with Fe dopant in the polymeric network.[23] Besides, no characteristic peaks for Fe were observed, suggesting that Fe was doped in the g-C_3N_4 skeleton. The surface chemical elemental states of the compound were analyzed, as shown in Fig. 2c–f. The XPS survey spectra (Fig. 2c) evidenced the existence of Fe in the prepared 0.054Fe/PCN. Besides, C and N were the primary elements in the two samples. The XPS results showed that the proportion of C/N atoms (Table S1†) in 0.054Fe/PCN increased compared with PCN, which may be due to the enhanced pore structures with Fe doping. Besides, the proportion variation also suggested the N atoms loss and polymerization improvement.[15] The C 1s XPS spectrum (Fig. 2d) was divided into two peaks located at 288.1 and 284.8 eV, corresponding to the sp^2-hybridized carbon in N=C–N and the defective C–C, respectively.[24,25] According to Table S2,† the percentage of defective C–C signal peak area for C 1s increased from 5.21% (PCN) to 11.49% (0.054Fe/

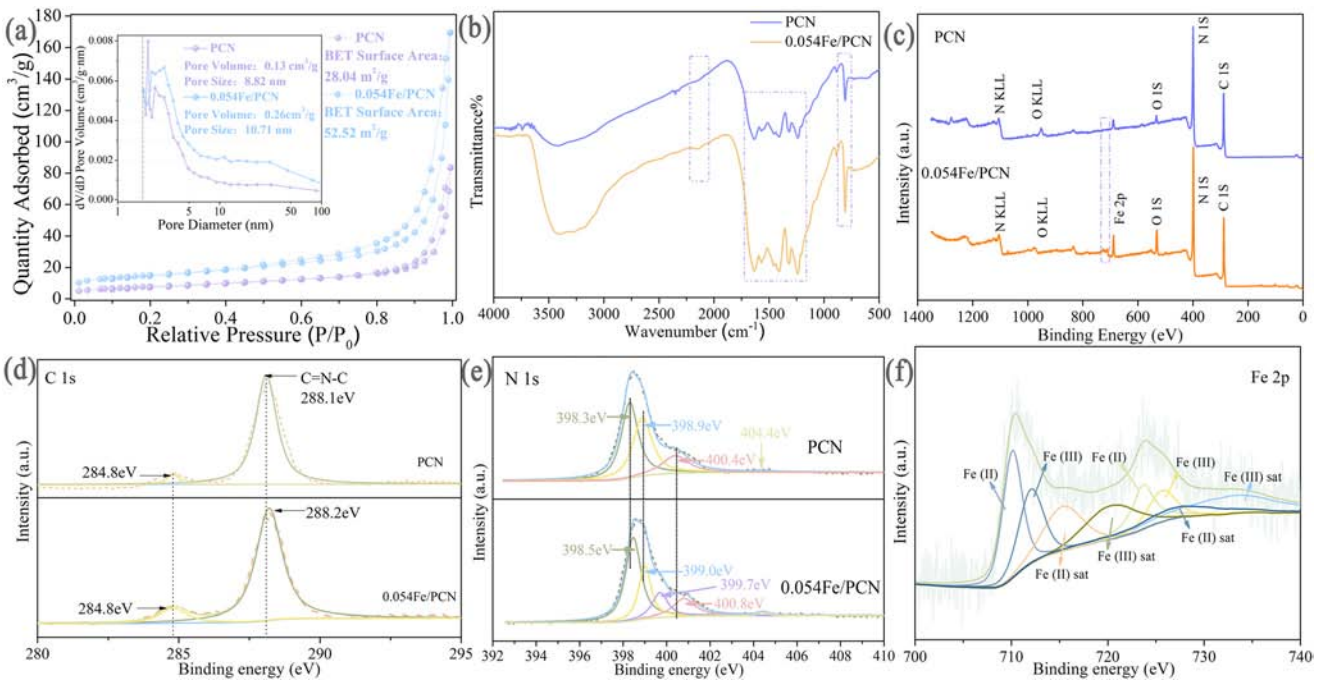

Fig. 2 (a) Nitrogen adsorption–desorption isotherms and pore size distribution plots (insert) of PCN and 0.054Fe/PCN. (b) FT-IR spectra of PCN and 0.054Fe/PCN. XPS spectra of PCN and 0.054Fe/PCN: (c) survey, (d) C 1s, (e) N 1s, and (f) Fe 2p.

PCN). This may be because Fe inhibited the polymerization of DCDA, and therefore the two-dimensional periodic regular arrangement of the heptazine ring was destroyed.[25] This is consistent with previous XRD results. Besides, in the N 1s XPS spectrum (Fig. 2e), the three strong peaks at 398.3, 398.9 and 400.4 eV of PCN are ascribed to sp^2-bonded N (C═N–C), N–$(C)_3$ and N–H_x, respectively.[26] Besides, the small peak at 404.4 eV is related to the π–π* excitations between the stacking interlayers.[27] The main peak (398.3 eV) was caused by the sp^2-bonded N atoms with lone pair electrons, which were more likely to capture Fe atoms with an empty orbit to form coordination bonds.[28] Moreover, a new signal peak at 399.7 eV in 0.054Fe/PCN (Fig. 2e) was observed, which corresponds to Fe–N bonds.[11,29,30] According to Table S3,† the content of Fe–N bonds based on the signal peak areas for N 1s increased with Fe doping. Besides, the peaks in 0.054Fe/PCN shifted to a higher binding energy compared to that of the PCN (Fig. 2d and e), which is probably due to the fact that the chemical state of the hybridized aromatic N changed after Fe modification.[31] The Fe atom with an empty orbit is attached to the N atom with a lone pair of electrons, resulting in a decrease in the density of the electron cloud around the N atom and associated C atom. Therefore, the nucleus is more tightly bound to the electron, resulting in a shift in the C 1s and N 1s orbitals towards a high binding energy.[32] Fig. 2f shows the Fe 2p XPS spectrum, where the two main asymmetric peaks at 710.7 and 724.6 eV for 0.054Fe/PCN belong to Fe 2p3/2 and Fe 2p1/2, respectively.[33] In the Fe 2p3/2 spectrum, the peak at 710.1 eV belongs to Fe(II), while the other peak at 712.1 eV is related to Fe(III).[34] In the spectrum of Fe 2p1/2, the peaks at 723.7 eV and 725.7 eV are related to Fe(II) and Fe(III), respectively. Besides, the presence of Fe(III) was also suggested by the shake-up satellite peaks at 720.7 eV and 733.6 eV, while the shake-up satellite peaks at 715.5 eV and 727.8 eV belong to Fe(II).[35] The above-mentioned results demonstrate that Fe was successfully coordinated with N atoms to form Fe–N moieties, which is in good agreement with the XRD analysis.

3.2 Photo-Fenton activity test

3.2.1 OTC degradation using different catalysts. The degradation of OTC was used to verify the catalytic properties of the prepared sample. According to Fig. S3,† OTC reached adsorption equilibrium after stirring for 30 min in the dark. Besides, Fig. S4† shows the OTC degradation result under different conditions, which shows that OTC was not degraded by photocatalysis in the absence of the catalyst, Fenton reagent, and photo-Fenton system. Besides, upon the addition of the catalyst, neither 0.054Fe/PCN nor PCN could effectively remove OTC *via* photocatalysis. In contrast, after the addition of H_2O_2 to the solution with 0.054Fe/PCN, the degradation slightly increased without irradiation. However, around 99.24% OTC was degraded after 60 min irradiation with H_2O_2, demonstrating that OTC was effectively degraded in the photo-Fenton system. This is likely because the catalyst was stimulated by the external conditions to produce radicals. Fig. 3a exhibits the photo-Fenton degradation efficiency for OTC by the prepared samples. The absorbance spectra of OTC (Fig. S5†) suggest that 0.054Fe/PCN exhibited an excellent performance for the removal of OTC. In contrast, only 6.27% OTC was degraded without the catalyst after 60 min irradiation. In the case of PCN, about 26.76% of OTC was removed. Compared with the results of photocatalysis (40.08%), the decreased removal may be owing to the fact that H_2O_2 may compete with the pollutants for adsorption sites.[36] The photo-Fenton degradation efficiency of OTC increased after Fe-doping. Consequently, the OTC removal efficiency reached as high as 99.24% with 0.054Fe/PCN. Fig. S6† shows the photo-Fenton degradation kinetics of OTC, and the rate constant of 0.054Fe/PCN was up to 0.076 min^{-1}. Besides, the degradation performance for other organics is exhibited in Fig. S7.† In addition, the comparison between 0.054Fe/PCN and other reported catalysts is listed in Table S4,† where 0.054Fe/PCN exhibited a superior catalytic activity for the degradation of OTC with a low consumption of H_2O_2.

3.2.2 OTC degradation using different H_2O_2 dosages. The effect of different H_2O_2 dosages on the degradation of OTC is exhibited in Fig. 3b. The OTC degradation efficiency was about 90.12% and 99.24% in the presence of 5 mmol and 0.5 mmol H_2O_2, respectively. Initially, 5 mmol H_2O_2 showed a better degradation efficiency, which was because more ·OH was generated in the high H_2O_2 dosage. However, excess H_2O_2 may compete with OTC for the adsorption sites on the catalyst surface. Therefore, 0.5 mmol H_2O_2 was optimal to utilize in these experiments. Besides, different H_2O_2 concentrations were also studied. Compared with 1 M H_2O_2, 10 M H_2O_2 showed a worse OTC degradation performance, which is ascribed to the fact that ·OH was scavenged by the high H_2O_2 concentration. Also, a high concentration might cause errors in the experiment owing to the lack of buffering force. Hence, 0.5 mL of 1 M H_2O_2 was chosen in this experiment.

3.2.3 Effects of different pH on degradation of OTC. Different pH affects the speciation of iron and H_2O_2 decomposition in Fenton-like systems. Acidic condition is conductive to the oxidation of organics, and thus more research is needed to explore high efficiency in a wide pH range. Fig. 3c shows the OTC degradation efficiency at different pH values. Under acidic conditions, the photo-Fenton system removal efficiency was higher, which reached 94.6% (pH = 3) and 93.9% (pH = 5). Under neutral and alkaline conditions, the OTC removal efficiency at pH = 7 and 9 was 74.5% and 74.3%, respectively. The oxidation potential of ·OH under basic media is lower, and therefore H_2O_2 is rapidly decomposed into O_2 and H_2O at high pH, and then the OTC degradation efficiency is low.[33] According to the results, although the degradation of OTC was more rapid under acidic conditions, it could also be efficiently degraded in alkaline conditions, suggesting that 0.054Fe/PCN possesses strong stability and corrosion resistance. This is because the formation of Fe–N bonds in 0.054Fe/PCN accelerated

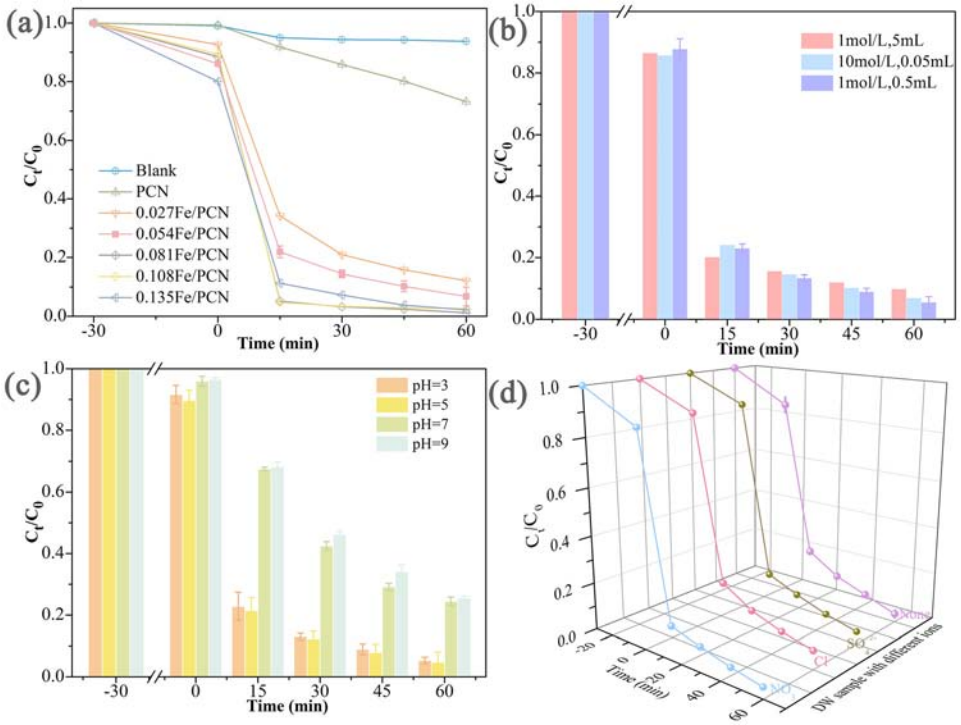

Fig. 3 (a) Degradation efficiency of OTC by PCN and *x*Fe/PCN composites in photo-Fenton system. (b) Effect of different concentrations and volumes of hydrogen peroxide on the degradation of OTC. Impact of (c) different pH and (d) inorganic salt ions (10 mM) on OTC degradation.

the migration iron and prevented the precipitation of iron salts under neutral and alkaline conditions.

3.2.4 Effects of different inorganic salt ions on degradation of OTC. In addition, inorganic salt ions widely exist in actual water bodies. Therefore, we studied the impact of common inorganic salt ions on the removal of OTC, including NO_3^-, Cl^-, SO_4^{2-} and CO_3^{2-}. As shown in Fig. 3d, there was no obvious negative effect on the removal of OTC in the presence of NO_3^-, Cl^- and SO_4^{2-}. Besides, Fig. S8† indicates that these three ions had no significant effect on

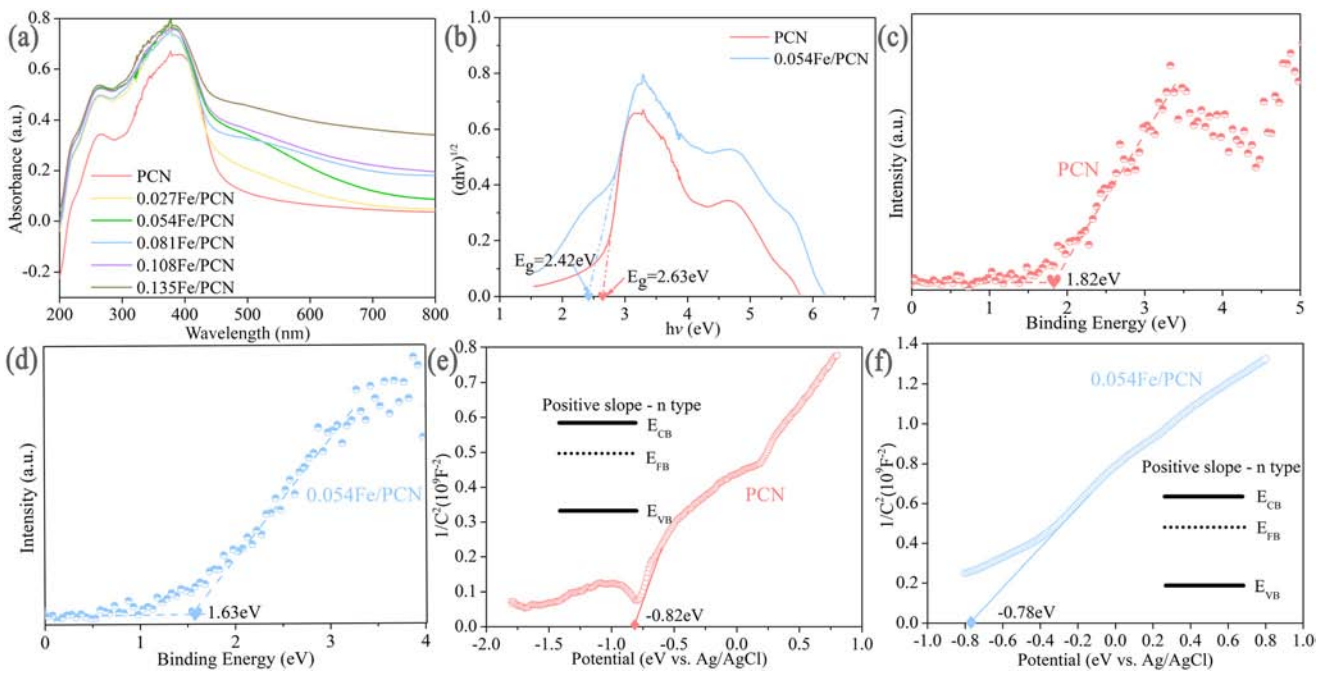

Fig. 4 (a) UV-vis absorption spectra of the prepared compound; (b) band gap energy of PCN and 0.054Fe/PCN; (c) VB XPS spectra of PCN and 0.054Fe/PCN (d); M–S analysis of PCN (e) and 0.054Fe/PCN (f) (conditions: 0.5 M of Na_2SO_4 electrolyte; pH: 5.96).

the removal of OTC at either low or high concentrations. However, CO_3^{2-} showed an obvious negative effect on the degradation of OTC (about 27% reduction rate). On the one hand, CO_3^{2-} could be used as hydroxyl radical quenchers;[37] on the other hand, the hydrolysis of CO_3^{2-} may cause the solution to become weakly alkalescent. Therefore, the removal efficiency of OTC decreased when the concentration of CO_3^{2-} was high. Hence, 0.054Fe/PCN exhibited strong anti-interference properties in the photo-Fenton system.

3.3 Photocatalysis-Fenton mechanism

3.3.1 Optical and electrical characteristic. The optical characteristics of the prepared catalyst were demonstrated by UV-vis DRS, as shown in Fig. 4a. The light absorption was enhanced following Fe doping. The response edge of PCN was observed to be about 450 nm, which was larger than that of the pristine g-C_3N_4 (420 nm). This can be attributed to the fact that hydrothermal-treated dicyandiamide can be used as an oxygen-containing precursor and show a wider visible light-response range.[15] Fe doping caused the absorption to be red-shifted, indicating the more effective utilization of solar energy. According to the formula $\alpha h\nu = A(h\nu - E_g)^{n/2}$ and the UV-vis DRS data, the bandgap of PCN and 0.054Fe/PCN was about 2.63 eV *vs.* NHE and 2.42 eV *vs.* NHE, respectively (Fig. 4b). Besides, the XPS results (Fig. 4c and d) revealed that the E_{VB} of PCN and 0.054Fe/PCN is around 1.82 eV *vs.* NHE and 1.63 eV *vs.* NHE, respectively. According to the formula $E_{CB} = E_{VB} - E_g$, the E_{CB} of PCN and 0.054Fe/PCN is −0.81 eV *vs.* NHE and −0.79 eV *vs.* NHE, which are more positive than that of $O_2/{}^{\bullet}O_2^-$ (−0.33 eV *vs.* NHE).

A Mott–Schottky experiment was performed to test the flat band potential of the composites. Firstly, both PCN and 0.054Fe/PCN were found to be n-type semiconductors, as proven by their positive plots (Fig. 4e and f, respectively).[38] Secondly, their flat band potential (E_{FB}) could be extrapolated from the *x*-intercept. The previous reports proved that in n-type semiconductors, E_{FB} equaled E_{CB}.[39,40] Therefore, the E_{CB} of PCN and 0.054Fe/PCN is approximately −0.82 eV *vs.* NHE and −0.78 eV *vs.* NHE, respectively. This is consistent with the results from VB XPS and UV-vis DRS.

Fig. 5a shows the PL analysis of PCN and 0.054Fe/PCN. PCN exhibited a high-intensity fluorescence peak at 460 nm and the fluorescence intensity of 0.054Fe/PCN was reduced by 75% compared to PCN. This indicates that the recombination rate between the photo-induced carriers of PCN was very high and doping Fe effectively restrained the recombination. Electrons can be transferred to Fe to accelerate the mobility of charge carriers and suppress electron–hole recombination. The EIS plots (Fig. 5b) were used to further verify the charge transfer efficiency. The radius of the Nyquist curve of 0.054Fe/PCN is smaller than that of PCN, suggesting its lower interfacial charge transfer resistance.[41] Doping Fe improved the interfacial charge carrier transport of the catalyst. Also, the radius of the Nyquist curve of 0.054Fe/PCN became smaller after the addition of H_2O_2, demonstrating faster electron transfer. Fig. 5c shows the photocurrent-time measurement (IT) of

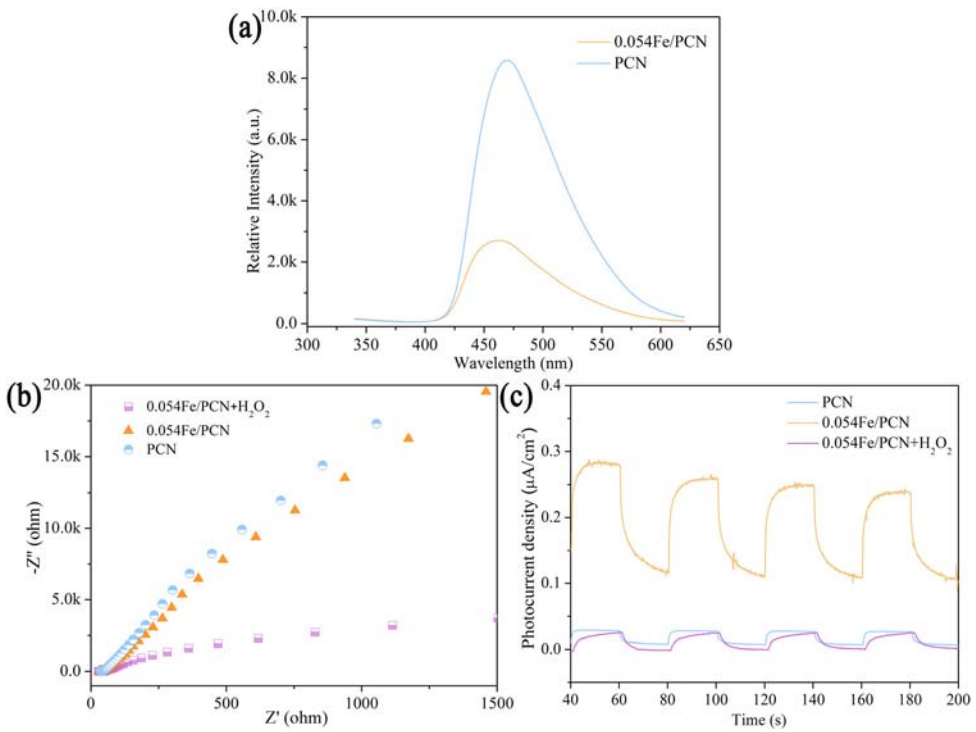

Fig. 5 (a) PL spectra, (b) EIS analysis and (c) transient photocurrent–time response curves of PCN and 0.054Fe/PCN (conditions: 0.5 M of Na_2SO_4 electrolyte; pH: 5.96; H_2O_2 = 5 mM).

PCN and 0.054Fe/PCN, illustrating the obvious transient photocurrent response of the samples. Compared with PCN, 0.054Fe/PCN showed a stronger photocurrent intensity with irradiation, revealing the enhanced separation and transportation of e^- and h^+, which is consistent with the above-mentioned PL result. The photocurrent response ability was reduced when H_2O_2 was added to 0.054Fe/PCN. Photo-induced electrons may take part in the Fenton reaction to form Fe(II) rather than migrate to the counter electrode through the external circuit. Fig. S9† also exhibits the photocurrent responses of PCN + H_2O_2. After visible-light illumination, PCN + H_2O_2 showed a stronger photocurrent intensity. Hence, the photo-induced e^- could be captured by H_2O_2. According to the PL, EIS and IT analysis, the photo-produced electrons transfer and consumption were improved due to Fe doping, resulting in the low recombination of electrons and holes.

3.3.2 Identification of radical species. Radical species play important role in the degradation of pollutants. Thus, the ESR/DMPO spin trap technique and radical scavenger experiments were performed to identify the radical species produced in the photo-Fenton oxidation process. Fig. 6a and b show the DMPO/$^{\cdot}OH$ and DMPO/$^{\cdot}O_2^-$ signals of 0.054Fe/PCN in the photo-Fenton system, which could promote the catalytic performance in the reaction. Combined with the free radical scavenging experiment (Fig. 6c), the OTC degradation efficiency decreased with the addition of TBA. Therefore, $^{\cdot}OH$ contributed to the degradation of OTC. Similarly, the degradation of OTC was also restrained greatly after the addition of TEMPO. This suggested that $^{\cdot}O_2^-$ radical played a dominant role in the reaction. In addition, SO–2Na was used to test the produced h^+, which was also conductive to OTC degradation in this photo-Fenton system. The ESR analysis and scavenger experiments indicated that radical species played an important role in the degradation of OTC. The specific mechanism of action is shown in the following section.

3.3.3 Possible mechanism of the enhanced photo-Fenton catalytic oxidation activity. The possible degradation mechanism for OTC is proposed in Fig. 7 according to the above-mentioned analysis. Specifically, 0.054Fe/PCN can be excited to produce h^+ and e^- under irradiation, where h^+ can directly oxidize OTC and e^- participates in other processes to produce more radicals. As shown in Fig. S10,† the signal intensity of DMPO/$^{\cdot}OH$ in the 0.054Fe/PCN photo-Fenton system was higher than that of PCN. Therefore, the possible $^{\cdot}OH$ generation processes are illustrated below. On the one hand, photo-induced e^- directly reacts with H_2O_2 to generate $^{\cdot}OH$. According to Fig. S9,† the obvious photocurrent response after visible-light illumination confirms that PCN + H_2O_2 could capture photo-induced e^-. Then, the photo-induced e^- reacts with H_2O_2 to generate $^{\cdot}OH$ in the photo-Fenton system.[11,42] On the other hand, photo-induced e^- may take part in the Fenton reaction to form Fe(II) and further produce $^{\cdot}OH$. Under the excitation of light, some e^- can transfer to Fe(III) *via* the Fe–N bond to produce Fe(II). Then, Fe(II) reacts with H_2O_2 to form $^{\cdot}OH$ and Fe(III).[43] During the whole process, Fe(III) and Fe(II) form an efficient cycle, which improves the degradation efficiency of the traditional Fenton reaction and solves the secondary

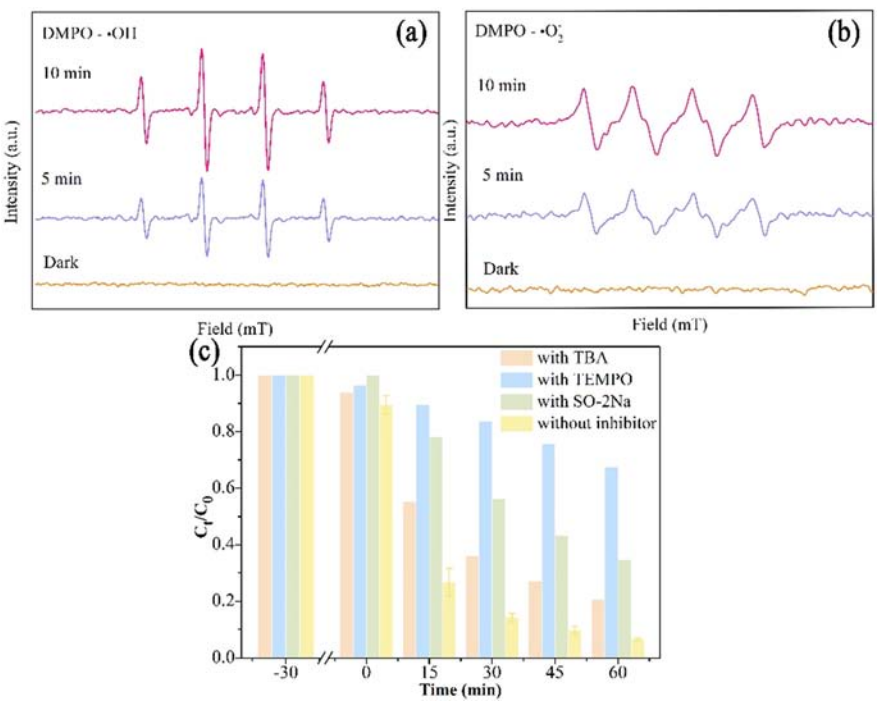

Fig. 6 ESR spectra of 0.054Fe/PCN by DMPO spin-trapping: (a) DMPO–$^{\cdot}OH$ and (b) for DMPO–$^{\cdot}O_2^-$ in the dark and under visible-light irradiation and (c) scavenger experiment: 100 mL 10 mg L^{-1} OTC solution with 10 mM TEMPO or 10 mM SO–2Na or 5 mL TBA scavengers.

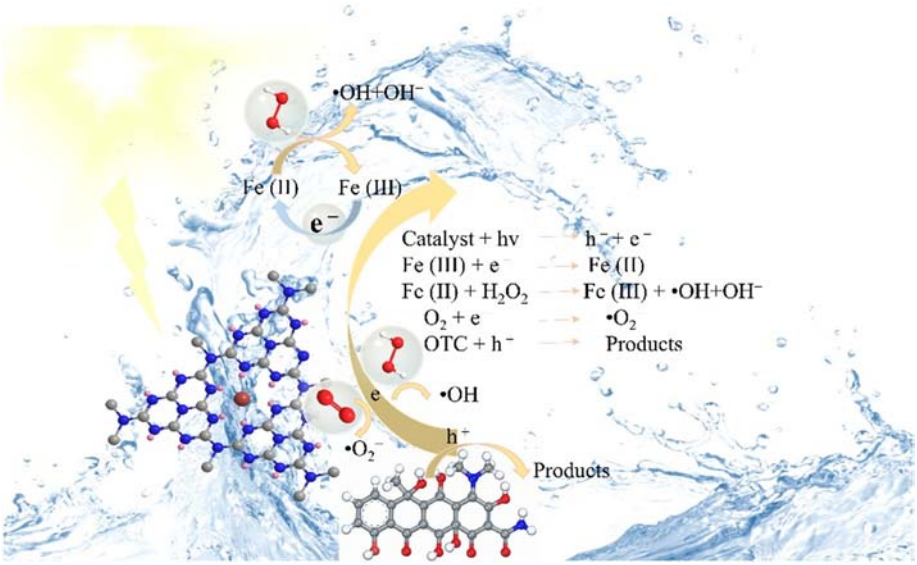

Fig. 7 Schematic illustration of the possible degradation mechanism by 0.054Fe/PCN.

pollution problem of iron sludge. Besides, the CB of 0.054Fe/PCN (−0.79 eV *vs.* NHE) is more positive than that of $O_2/{}^{\bullet}O_2^-$ (−0.33 eV *vs.* NHE), and therefore the dissolved oxygen will capture e^- to generate ${}^{\bullet}O_2^-$ to react with OTC.[13] Doping Fe in PCN enhances the activation of H_2O_2 by forming Fe–N sites, endowing 0.054Fe/PCN with excellent properties for the degradation of OTC. This can be related to the rapid regeneration of Fe(II) species by the photo-induced e^- from the surrounding PCN network.[5]

3.3.4 Identification of pathway in OTC degradation. To understand the pathway of OTC degradation, LC-MS was used to detect the degradation intermediates. The intense peak with the *m*/*z* of 461.1 (OTC) disappeared after 60 min (Fig. S11†), suggesting the successive attacks for OTC. The typical intermediates are displayed in Table S5† and Fig. 8 presents the two possible main degradation pathways. According to the relevant reports and the detected intermediates, P2 was generated through *N*-demethylation,

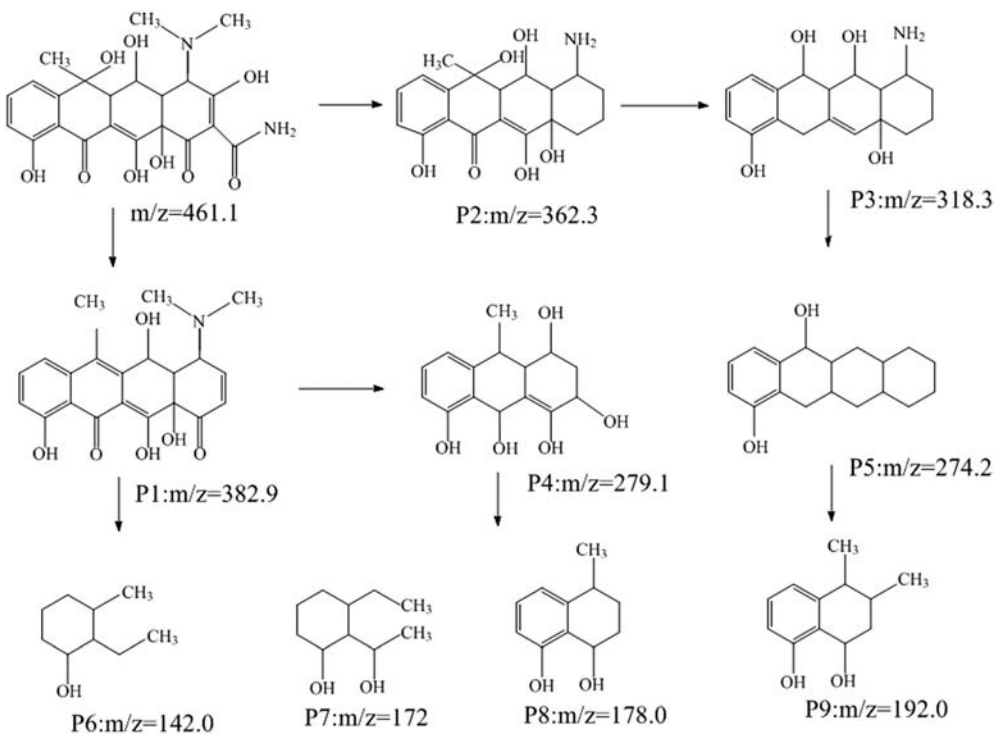

Fig. 8 Possible degradation processes of OTC by 0.054Fe/PCN.

decarbonylation, dihydroxylation and deamidation.[2] Then, P2 was attacked through demethylation and decarbonylation to generate P3. Holes played an important role in the *N*-demethylation process,[44] while in dehydration and hydroxylation process, $^{\cdot}OH$ was the primary attacker. P3 was transformed to P5 *via* deamination and dehydroxylation. Meanwhile, OTC could be attacked *via* abscission of the acetyl group, dehydroxylation, and dehydration to transform P1. Subsequently, P1 could be decomposed to P4 by dehydroxylation. These intermediates were further oxidized to generate P6, P7, P8 and P9. Therefore, OTC was verified to degrade over 0.054Fe/PCN.

3.3.5 Toxicity simulation analysis. The toxicity of OTC and its by-products may cause an environmental risk; therefore, it is necessary to determine the toxicity of the predicted intermediates of OTC. Accordingly, the Toxicity Estimation Software Tool (TEST) was used to simulate the toxicity of the intermediate products. There were 6 significant models including fathead minnow LC50-96 h, *Daphnia magna* LC50-48 h, oral rat LD50, bioconcentration, developmental toxicity and mutagenicity to verify the reduction in toxicity based on the quantitative structure–activity relationship analysis.[45] The fathead minnow LC50-96 h value for OTC was about 1.12 mg L^{-1}. Because of their large value with less harm,[46] the intermediate products showed a high value but less acute toxicity (Fig. 9a). Fig. S12a† also exhibits the *Daphnia magna* LC50-48 h values, which exhibit the same trend as the fathead minnow LC50-96 h values. Besides, as shown in Fig. 9b, the oral rat LD50 value was 1140.02 mg kg^{-1}, while the final intermediates (P8 and P9) reached 2699.74 and 1971.41 mg kg^{-1}, respectively, showing lower harm. Additionally, after degradation, most of the intermediates showed weak ecological enrichment effects because the bioconcentration factor was less than 5 (Fig. 9c). Although the developmental toxicity values of the intermediates were not listed as "developmental non-toxicity", most of them were lower than that of OTC (Fig. S12b†). In addition, the mutagenicity was also studied (Fig. 9d). It was found that the mutagenicity of almost all the intermediates was less negative than that of OTC. Therefore, the degradation process may prevent secondary pollution and be recognized as green technology.

3.4 Stability of synthesized catalyst

0.054Fe/PCN also exhibited excellent stability and recyclability. Firstly, the cyclic experiments for the degradation of OTC are shown in Fig. 10a. 0.054Fe/PCN was reused in multiple degradation runs. The results showed that after four cycles, the high OTC degradation efficiency was still maintained at 82.4%. The decline in the degradation rate from 99.2% to 82.4% is probably due to the leaching of a small amount of iron (446.8 μg L^{-1}), resulting in the loss of some active sites. This also poses a challenge for us to inhibit iron leaching later on. Besides, some residual contamination on the surface also affected the degradation, which could be observed from decreased adsorption performance. After two cycles, the photo-Fenton catalytic system achieved a steady performance in the following cycling runs. In addition, the used 0.054Fe/PCN was also characterized. There was no obvious variation in the XRD patterns (Fig. 10b), FTIR (Fig. 10c) and XPS spectra (Fig. 10d) of the fresh and used 0.054Fe/PCN, confirming its excellent stability. The detailed XPS spectra of C, N and Fe are shown in Fig. S13.† There were no distinct changes in the elemental composition and valence state of 0.054Fe/PCN. In contrast, for Fe, the content

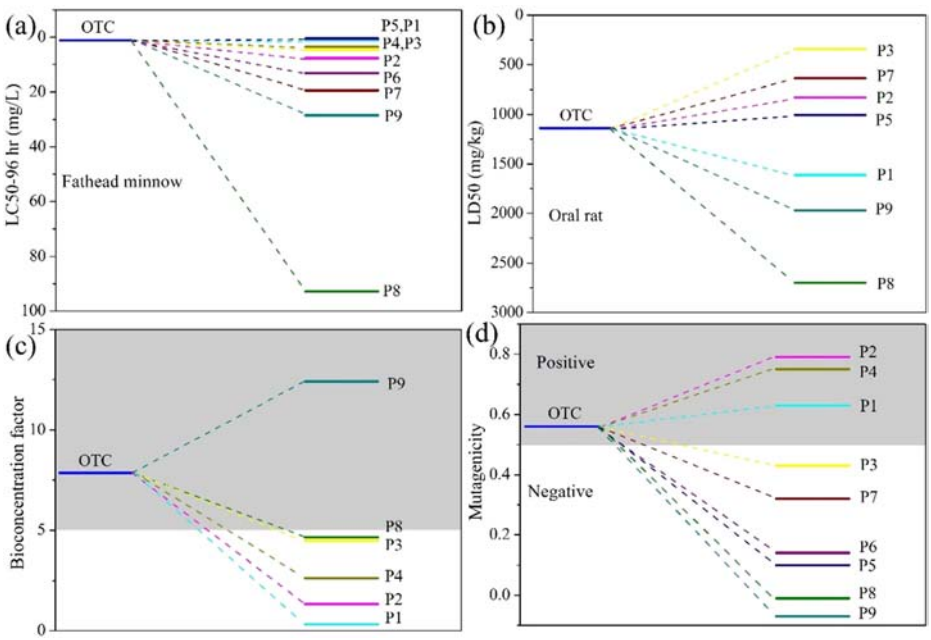

Fig. 9 (a) Fathead minnow LC50-96 h; (b) oral rat LD50, (c) bioconcentration factor and (d) mutagenicity of OTC and predictive intermediates.

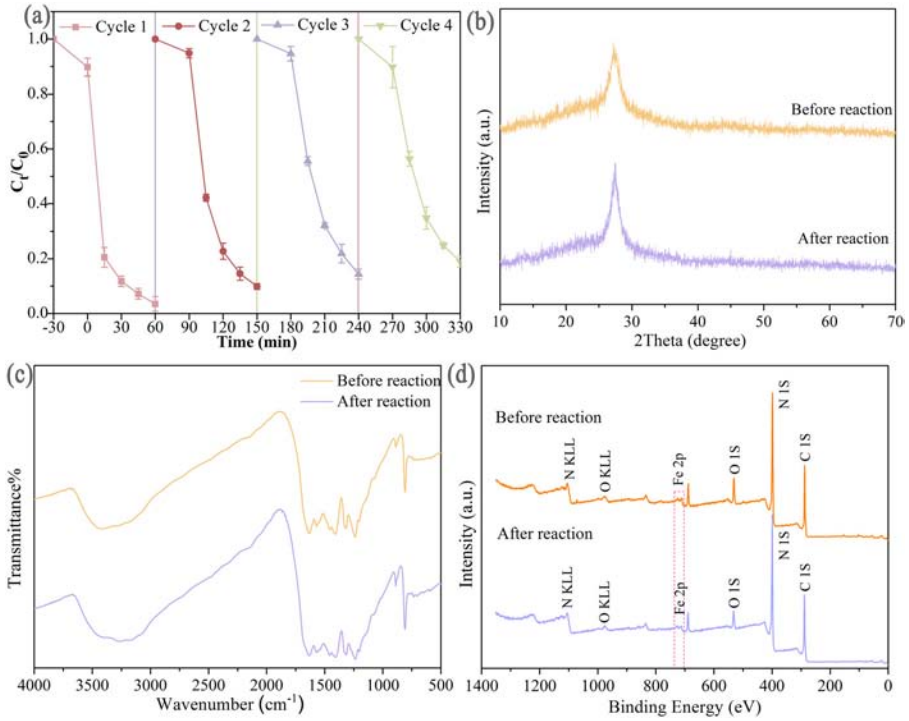

Fig. 10 (a) Catalytic activity of the used 0.054Fe/PCN, (b) XRD patterns, (c) FTIR spectra and (d) XPS survey spectra of fresh and used 0.054 Fe/PCN.

of Fe(II) was reduced from 28.81% to 24.28% after the reaction, which proved that Fe(II) was involved in this reaction. Especially, because of the decrease in Fe(II), the degradation of OTC dropped, which is consistent with the cyclic experimental results. Moreover, the percentage of Fe(II) in the recycled 0.054Fe/PCN was also high according to the XPS analysis owing to the accelerated circulation of the Fe(III)/Fe(II) pair by photogenerated electrons, which prevented the precipitation of iron salts. Besides, the morphology analysis is shown in Fig. S14.† In general, there was no obvious variation and the stability of 0.054Fe/PCN was excellent for actual application.

4. Conclusion

In conclusion, Fe-doped porous g-C_3N_4 was synthesized *via* a one-step self-assembly strategy. SEM, TEM and BET were used to determine its morphology and pore volume. The synthesized 0.054Fe/PCN exhibited a high catalytic performance in the photo-Fenton system, as follows: i) the porous structure with a large surface area provided abundant active sites; ii) the photo-induced e^- could react with dissolved O_2 and Fe(III) to form $^{\bullet}O_2^-$ and Fe(II); and iii) the converted Fe(II) could react with H_2O_2 to produce $^{\bullet}OH$ and regenerate Fe(III). Therefore, 99.24% OTC was degraded over 0.054Fe/PCN within 60 min in the photo-Fenton system, while PCN only exhibited 26.8% degradation under the same conditions. The possible degradation pathway was proposed based on the identification of the radical species, and the TEST analysis confirmed that this degradation progress is environmental-friendly. Especially, the synthesized 0.054Fe/PCN worked effectively in a wide pH range and showed strong anti-interference capability. Besides, the great stability and reusability of this catalyst make it a potential candidate for actual application. Thus, a new strategy is proposed in this work to synthesize efficient catalysts to realize environment remediation in photo-Fenton systems.

Author contributions

Xiuqin Huo: conceptualization, investigation, visualization, writing-original draft. Huan Yi: investigation, writing-original draft, funding acquisition. Eydhah Almatrafi: investigation, writing-original draft. Dengsheng Ma: methodology, writing-review & editing. Yukui Fu: methodology, formal analysis, writing-review & editing. Lei Qin: conceptualization, writing-review & editing. Wu Xia: validation, writing-review & editing. Ling Xiang: methodology, writing – review & editing. Fuhang Xu: writing-review & editing. Huchuan Yan: writing-review & editing. Chengyun Zhou: writing-review & editing. Guangming Zeng: conceptualization, writing – review & editing, project administration, supervision, funding acquisition. Cui Lai: conceptualization, methodology, writing – review & editing, resources, supervision, funding acquisition.

Conflicts of interest

The authors declare that they have no known competing financial interests or personal relationships that could have appeared to influence the work reported in this paper.

Acknowledgements

This study was financially supported by the Program for the National Natural Science Foundation of China (U20A20323, 51521006, 51879101, 51579098, 51779090, 52100183, 52170161), the National Program for Support of Top-Notch Young Professionals of China (2014), and Hunan Natural Science Foundation (2020JJ3009), Hunan Researcher Award Program (2020RC3025), the Science and Technology Innovation Program of Hunan Province (2021RC2057), the Project funded by China Postdoctoral Science Foundation (2021M700041), Changsha Municipal Natural Science Foundation (kq2202166), and the Fundamental Research Funds for the Central Universities (531119200086, 531118010114, 531118040083, 541109060031, 531118010473).

References

1 R. Ding, W. Yan, Y. Wu, Y. Xiao, H. Gang, S. Wang, L. Chen and F. Zhao, Light-excited photoelectrons coupled with bio-photocatalysis enhanced the degradation efficiency of oxytetracycline, *Water Res.*, 2018, **143**, 589–598.

2 Y. Yang, G. Zeng, D. Huang, C. Zhang, D. He, C. Zhou, W. Wang, W. Xiong, B. Song, H. Yi, S. Ye and X. Ren, In Situ Grown Single-Atom Cobalt on Polymeric Carbon Nitride with Bidentate Ligand for Efficient Photocatalytic Degradation of Refractory Antibiotics, *Small*, 2020, **16**, 2001634.

3 W. Yan, Y. Guo, Y. Xiao, S. Wang, R. Ding, J. Jiang, H. Gang, H. Wang, J. Yang and F. Zhao, The changes of bacterial communities and antibiotic resistance genes in microbial fuel cells during long-term oxytetracycline processing, *Water Res.*, 2018, **142**, 105–114.

4 T. Jia, J. Wu, Z. Ji, C. Peng, Q. Liu, M. Shi, J. Zhu, H. Wang, D. Liu and M. Zhou, Surface defect engineering of Fe-doped $Bi_7O_9I_3$ microflowers for ameliorating charge-carrier separation and molecular oxygen activation, *Appl. Catal., B*, 2021, **284**, 119727.

5 J. Hu, P. Zhang, W. An, L. Liu, Y. Liang and W. Cui, In-situ Fe-doped g-C_3N_4 heterogeneous catalyst via photocatalysis-Fenton reaction with enriched photocatalytic performance for removal of complex wastewater, *Appl. Catal., B*, 2019, **245**, 130–142.

6 H. Yi, C. Lai, X. Huo, L. Qin, Y. Fu, S. Liu, L. Li, M. Zhang, M. Chen and G. Zeng, H2O2-free photo-Fenton system for antibiotics degradation in water via the synergism of oxygen-enriched graphitic carbon nitride polymer and nano manganese ferrite, *Environ. Sci.: Nano*, 2022, **9**, 815–826.

7 D. Ma, H. Yi, C. Lai, X. Liu, X. Huo, Z. An, L. Li, Y. Fu, B. Li, M. Zhang, L. Qin, S. Liu and L. Yang, Critical review of advanced oxidation processes in organic wastewater treatment, *Chemosphere*, 2021, **275**, 130104.

8 X. Huo, Y. Yang, Q. Niu, Y. Zhu, G. Zeng, C. Lai, H. Yi, M. Li, Z. An, D. Huang, Y. Fu, B. Li, L. Li and M. Zhang, A direct Z-scheme oxygen vacant BWO/oxygen-enriched graphitic carbon nitride polymer heterojunction with enhanced photocatalytic activity, *Chem. Eng. J.*, 2021, **403**, 126363.

9 Z. Wei, M. Liu, Z. Zhang, W. Yao, H. Tan and Y. Zhu, Efficient visible-light-driven selective oxygen reduction to hydrogen peroxide by oxygen-enriched graphitic carbon nitride polymers, *Energy Environ. Sci.*, 2018, **11**, 2581–2589.

10 S. Liu, C. Lai, B. Li, X. Liu, X. Zhou, C. Zhang, L. Qin, L. Li, M. Zhang, H. Yi, Y. Fu, H. Yan and L. Chen, Heteroatom doping in metal-free carbonaceous materials for the enhancement of persulfate activation, *Chem. Eng. J.*, 2022, **427**, 131655.

11 W. Miao, Y. Liu, X. Chen, Y. Zhao and S. Mao, Tuning layered Fe-doped g-C_3N_4 structure through pyrolysis for enhanced Fenton and photo-Fenton activities, *Carbon*, 2020, **159**, 461–470.

12 C. Lai, D. Ma, H. Yi, M. Zhang, F. Xu, X. Huo, H. Ye, L. Li, L. Yang, L. Tang and M. Yan, Functional partition of Fe and Ti co-doped g-C3N4 for photo-Fenton degradation of oxytetracycline: Performance, mechanism, and DFT study, *Sep. Purif. Technol.*, 2023, **306**, 122546.

13 S. Liu, D. Liu, Y. Sun, P. Xiao, H. Lin, J. Chen, X.-L. Wu, X. Duan and S. Wang, Enzyme-mimicking single-atom FeN4 sites for enhanced photo-Fenton-like reactions, *Appl. Catal., B*, 2022, **310**, 121327.

14 X. Huo, H. Yi, Y. Fu, Z. An, L. Qin, X. Liu, B. Li, S. Liu, L. Li, M. Zhang, F. Xu, G. Zeng and C. Lai, Porous graphitic carbon nitride nanomaterials for water treatment, *Environ. Sci.: Nano*, 2021, **8**, 1835–1862.

15 J. Zhang, Y. Huang, T. Nie, R. Wang, B. He, B. Han, H. Wang, Y. Tian and Y. Gong, Enhanced visible-light photocatalytic H_2 production of hierarchical g-C_3N_4 hexagon by one-step self-assembly strategy, *Appl. Surf. Sci.*, 2020, **499**, 143942.

16 Y. Xu, F. Ge, Z. Chen, S. Huang, W. Wei, M. Xie, H. Xu and H. Li, One-step synthesis of Fe-doped surface-alkalinized g-C_3N_4 and their improved visible-light photocatalytic performance, *Appl. Surf. Sci.*, 2019, **469**, 739–746.

17 F. Xu, C. Lai, M. Zhang, B. Li, S. Liu, M. Chen, L. Li, Y. Xu, L. Qin, Y. Fu, X. Liu, H. Yi and X. Yang, Facile one-pot synthesis of carbon self-doped graphitic carbon nitride loaded with ultra-low ceric dioxide for high-efficiency environmental photocatalysis: Organic pollutants degradation and hexavalent chromium reduction, *J. Colloid Interface Sci.*, 2021, **601**, 196–208.

18 Y. Wang, L. Li, Y. Wei, J. Xue, H. Chen, L. Ding, J. Caro and H. Wang, Water Transport with Ultralow Friction through Partially Exfoliated g-C_3N_4 Nanosheet Membranes with Self-Supporting Spacers, *Angew. Chem., Int. Ed.*, 2017, **56**, 8974–8980.

19 E. da Cruz Severo, G. L. Dotto, A. Martínez-de la Cruz, E. L. Cuellar and E. L. Foletto, Enhanced photocatalytic activity of $BiVO_4$ powders synthesized in presence of EDTA for the decolorization of rhodamine B from aqueous solution, *Environ. Sci. Pollut. Res.*, 2018, **25**, 34123–34130.

20 Y. Fu, T. Huang, L. Zhang, J. Zhu and X. Wang, Ag/g-C_3N_4 catalyst with superior catalytic performance for the degradation of dyes: a borohydride-generated superoxide radical approach, *Nanoscale*, 2015, **7**, 13723–13733.

21 W.-D. Oh, L.-W. Lok, A. Veksha, A. Giannis and T.-T. Lim, Enhanced photocatalytic degradation of bisphenol A with Ag-decorated S-doped g-C_3N_4 under solar irradiation: Performance and mechanistic studies, *Chem. Eng. J.*, 2018, **333**, 739–749.

22 Z. Yang, X. Xu, X. Liang, C. Lei, Y. Cui, W. Wu, Y. Yang, Z. Zhang and Z. Lei, Construction of heterostructured MIL-125/Ag/g-C_3N_4 nanocomposite as an efficient bifunctional visible light photocatalyst for the organic oxidation and reduction reactions, *Appl. Catal., B*, 2017, **205**, 42–54.

23 W.-D. Oh, C.-Z. Ng, S.-L. Ng, J.-W. Lim and K.-H. Leong, Rapid degradation of organics by peroxymonosulfate activated with ferric ions embedded in graphitic carbon nitride, *Sep. Purif. Technol.*, 2020, **230**, 115852.

24 C. Lai, Z. An, H. Yi, X. Huo, L. Qin, X. Liu, B. Li, M. Zhang, S. Liu, L. Li, Y. Fu, X. Zhou, Z. Wang, N. An and X. Shi, Enhanced visible-light-driven photocatalytic activity of bismuth oxide via the decoration of titanium carbide quantum dots, *J. Colloid Interface Sci.*, 2021, **600**, 161–173.

25 X. Wang and Z. Nan, Highly efficient Fenton-like catalyst Fe-g-C3N4 porous nanosheets formation and catalytic mechanism, *Sep. Purif. Technol.*, 2020, **233**, 116023.

26 H. Gao, R. Cao, S. Zhang, H. Yang and X. Xu, Three-Dimensional Hierarchical g-C_3N_4 Architectures Assembled by Ultrathin Self-Doped Nanosheets: Extremely Facile Hexamethylenetetramine Activation and Superior Photocatalytic Hydrogen Evolution, *ACS Appl. Mater. Interfaces*, 2019, **11**, 2050–2059.

27 H. Li, C. Shan and B. Pan, Fe(III)-Doped g-C3N4 Mediated Peroxymonosulfate Activation for Selective Degradation of Phenolic Compounds via High-Valent Iron-Oxo Species, *Environ. Sci. Technol.*, 2018, **52**, 2197–2205.

28 S. An, G. Zhang, T. Wang, W. Zhang, K. Li, C. Song, J. T. Miller, S. Miao, J. Wang and X. Guo, High-Density Ultra-small Clusters and Single-Atom Fe Sites Embedded in Graphitic Carbon Nitride (g-C_3N_4) for Highly Efficient Catalytic Advanced Oxidation Processes, *ACS Nano*, 2018, **12**, 9441–9450.

29 H. Sun, L. Wang, F. Guo, Y. Shi, L. Li, Z. Xu, X. Yan and W. Shi, Fe-doped g-C3N4 derived from biowaste material with Fe-N bonds for enhanced synergistic effect between photocatalysis and Fenton degradation activity in a broad pH range, *J. Alloys Compd.*, 2022, **900**, 163410.

30 J. Ma, Q. Yang, Y. Wen and W. Liu, Fe-g-C3N4/graphitized mesoporous carbon composite as an effective Fenton-like catalyst in a wide pH range, *Appl. Catal., B*, 2017, **201**, 232–240.

31 T. Ma, Q. Shen, B. Z. J. Xue, R. Guan, X. Liu, H. Jia and B. Xu, Facile synthesis of Fe-doped g-C_3N_4 for enhanced visible-light photocatalytic activity, *Inorg. Chem. Commun.*, 2019, **107**, 107451.

32 J. Gao, Y. Wang, S. Zhou, W. Lin and Y. Kong, A Facile One-Step Synthesis of Fe-Doped g-C_3N_4 Nanosheets and Their Improved Visible-Light Photocatalytic Performance, *ChemCatChem*, 2017, **9**, 1708–1715.

33 L. Li, S. Liu, M. Cheng, C. Lai, G. Zeng, L. Qin, X. Liu, B. Li, W. Zhang, Y. Yi, M. Zhang, Y. Fu, M. Li and M. Long, Improving the Fenton-like catalytic performance of MnOx-Fe_3O_4/biochar using reducing agents: A comparative study, *J. Hazard. Mater.*, 2021, **406**, 124333.

34 L. Qin, Z. Wang, Y. Fu, C. Lai, X. Liu, B. Li, S. Liu, H. Yi, L. Li, M. Zhang, Z. Li, W. Cao and Q. Niu, Gold nanoparticles-modified $MnFe_2O_4$ with synergistic catalysis for photo-Fenton degradation of tetracycline under neutral pH, *J. Hazard. Mater.*, 2021, **414**, 125448.

35 X. Wei, H. Yi, C. Lai, X. Huo, D. Ma and C. Du, Synergistic effect of flower-like $MnFe_2O_4/MoS_2$ on photo-Fenton oxidation remediation of tetracycline polluted water, *J. Colloid Interface Sci.*, 2022, **608**, 942–953.

36 L. Li, C. Lai, F. Huang, M. Cheng, G. Zeng, D. Huang, B. Li, S. Liu, M. Zhang, L. Qin, M. Li, J. He, Y. Zhang and L. Chen, Degradation of naphthalene with magnetic bio-char activate hydrogen peroxide: Synergism of bio-char and Fe–Mn binary oxides, *Water Res.*, 2019, **160**, 238–248.

37 M. Li, C. Lai, H. Yi, D. Huang, L. Qin, X. Liu, B. Li, S. Liu, M. Zhang, Y. Fu, L. Li, J. He, Y. Zhang and L. Chen, Multiple charge-carrier transfer channels of Z-scheme bismuth tungstate-based photocatalyst for tetracycline degradation: Transformation pathways and mechanism, *J. Colloid Interface Sci.*, 2019, **555**, 770–782.

38 S. Luo, J. Ke, M. Yuan, Q. Zhang, P. Xie, L. Deng and S. Wang, $CuInS_2$ quantum dots embedded in Bi_2WO_6 nanoflowers for enhanced visible light photocatalytic removal of contaminants, *Appl. Catal., B*, 2018, **221**, 215–222.

39 Q. Huo, X. Qi, J. Li, G. Liu, Y. Ning, X. Zhang, B. Zhang, Y. Fu and S. Liu, Preparation of a direct Z-scheme α-Fe2O3/MIL-101(Cr) hybrid for degradation of carbamazepine under visible light irradiation, *Appl. Catal., B*, 2019, **255**, 117751.

40 H. Yi, M. Yan, D. Huang, G. Zeng, C. Lai, M. Li, X. Huo, L. Qin, S. Liu, X. Liu, B. Li, H. Wang, M. Shen, Y. Fu and X. Guo, Synergistic effect of artificial enzyme and 2D nano-structured Bi_2WO_6 for eco-friendly and efficient biomimetic photocatalysis, *Appl. Catal., B*, 2019, **250**, 52–62.

41 K. C. Devarayapalli, S. V. P. Vattikuti, T. V. M. Sreekanth, K. S. Yoo, P. C. Nagajyothi and J. Shim, Hydrogen production and photocatalytic activity of g-C_3N_4/Co-MOF (ZIF-67) nanocomposite under visible light irradiation, *Appl. Organomet. Chem.*, 2020, **34**, e5376.

42 H. Yi, E. Almatrafi, D. Ma, X. Huo, L. Qin, L. Li, X. Zhou, C. Zhou, G. Zeng and C. Lai, Spatial confinement: A green pathway to promote the oxidation processes for organic pollutants removal from water, *Water Res.*, 2023, **233**, 119719.

43 Q. Liu, T. Chen, Y. Guo, Z. Zhang and X. Fang, Grafting Fe(III) species on carbon nanodots/Fe-doped g-C3N4 via interfacial charge transfer effect for highly improved photocatalytic performance, *Appl. Catal., B*, 2017, **205**, 173–181.

44 Y. Yang, Z. Zeng, C. Zhang, D. Huang, G. Zeng, R. Xiao, C. Lai, C. Zhou, H. Guo, W. Xue, M. Cheng, W. Wang and J. Wang, Construction of iodine vacancy-rich BiOI/Ag@AgI

Z-scheme heterojunction photocatalysts for visible-light-driven tetracycline degradation: Transformation pathways and mechanism insight, *Chem. Eng. J.*, 2018, **349**, 808–821.

45 P. Ding, H. Ji, P. Li, Q. Liu, Y. Wu, M. Guo, Z. Zhou, S. Gao, W. Xu, W. Liu, Q. Wang and S. Chen, Visible-light degradation of antibiotics catalyzed by titania/zirconia/graphitic carbon nitride ternary nanocomposites: a combined experimental and theoretical study, *Appl. Catal., B*, 2022, **300**, 120633.

46 P. Hong, Z. Wu, D. Yang, K. Zhang, J. He, Y. Li, C. Xie, W. Yang, Y. Yang, L. Kong and J. Liu, Efficient generation of singlet oxygen (1O2) by hollow amorphous Co/C composites for selective degradation of oxytetracycline via Fenton-like process, *Chem. Eng. J.*, 2021, **421**, 129594.